

1 Weakened Miocene Temperature Response to Orbital Forcing 2 Compared to the Modern-Day

3 Yurui Zhang^{1*}, Jilin Wei^{2,3}, Zhen Li¹, Nan Dai¹, Weipeng Zheng^{2,3,4}, Qiuzhen Yin⁵, Agatha M.
4 de Boer⁶, Zhengguo Shi^{7,8}, Lixia Zhang²

5 ¹State Key Laboratory of Marine Environmental Science, College of Ocean & Earth Sciences, Xiamen University,
6 Xiamen, China

7 ²State Key Laboratory of Earth System Numerical Modeling and Application, Institute of Atmospheric Physics,
8 Chinese Academy of Sciences, Beijing, China

9 ³College of Earth and Planetary Sciences, University of Chinese Academy of Sciences, Beijing, China

10 ⁴Earth System Numerical Simulation Science Center, Institute of Atmospheric Physics, Chinese Academy of
11 Sciences, Beijing, China

12 ⁵Earth and Climate Research Center, Earth and Life Institute, Universit  catholique de Louvain, Louvain-la-Neuve,
13 Belgium

14 ⁶Department of Geological Sciences, Bolin Centre for Climate Research, Stockholm University, Sweden

15 ⁷State Key Laboratory of Loess Science, Institute of Earth Environment, Chinese Academy of Sciences, Xi'an,
16 China

17 ⁸Institute of Global Environmental Change, Xi'an Jiaotong University, Xi'an, China

18
19 *Correspondence to:* Yurui Zhang (yuruizhang@xmu.edu.cn)

20 **Abstract.** Although orbital signal is widely identified in Miocene proxy records, the climate mechanisms linking
21 insolation changes to regional temperature within this warm, low-ice period remains not well known. Here we use
22 fully coupled climate model simulations to assess temperature response to maximum and minimum boreal summer
23 insolation under Miocene and pre-industrial (PI) conditions. Under both conditions, temperature exhibits broadly anti-
24 phased responses to increased and decreased insolation, but the Miocene response is overall weaker, with regionally
25 dependent contrasts and reduced symmetry between two orbital cases. Three notable Miocene-PI differences emerge:
26 (1) reduced boreal continental sensitivity in the Miocene due to dampened albedo, water-vapor and cloud feedbacks
27 in a warmer, low-ice climate; (2) stronger Miocene cooling over tropical North Africa under high insolation, driven
28 by intensified hydrological and moisture-feedbacks supported by a wider Tethys Sea; (3) reversed Southern Ocean
29 anomalies under low insolation, where poleward-restricted Miocene sea ice enables winter insolation changes to
30 trigger positive ice-albedo feedbacks. These results demonstrate that background climate state strongly modulates
31 orbital-scale responses and provide important context for interpreting Miocene proxy records and long-term changes
32 in Earth's climate sensitivity through the Neogene.

33 **1 Introduction**

34 The Miocene (~23 to 5.3 Ma) marks a pivotal stage in Earth's long-term Cenozoic cooling trajectory, characterized
35 by major reorganization of the cryosphere, monsoon systems and global climate (Steinthorsdottir et al., 2021). The
36 warmest interval of this epoch, the Miocene Climatic Optimum (MCO, ~17–14 Ma), was marked by globally
37 elevated temperatures, reduced meridional temperature gradients, limited Antarctic sea ice, and intensified
38 hydrological activity in the tropics and subtropics (Holbourn et al., 2013; Steinthorsdottir et al., 2021;) (Acosta et
39 al., 2024; Goldner et al., 2014; Burls et al., 2021). Following the MCO, the climate transitioned toward cooler
40 conditions, accompanied by stepwise expansion of Antarctic sea ice and intensified monsoons circulation (e.g.,
41 (Steinthorsdottir et al., 2021; Holbourn et al., 2013; Holbourn et al., 2018; Westerhold et al., 2020; Frigola et al.,
42 2021; Halberstadt et al., 2021). These large-scale reorganizations have been widely interpreted as responses to
43 changes in external forcing acting on an evolving climate background state.

44 A growing body of evidence links these Miocene climate changes to orbital forcing, through mechanisms involving
45 Antarctic ice-sheet dynamics (Levy et al., 2019; Naish et al., 2009) and eccentricity-paced variations in the marine
46 carbon cycle associated with an intensified tropical hydrological cycle (Holbourn et al., 2007; Liu et al., 2024; Tian
47 et al., 2013). Long-term marine records further indicate that the sensitivity of Antarctic ice sheets to obliquity
48 forcing intensified from the Miocene onward and persisted into the Pliocene and Pleistocene (Levy et al., 2019; Van
49 Peer et al., 2024). Spectral analyses of benthic $\delta^{18}\text{O}$ and $\delta^{13}\text{C}$ records show dominant 400 kyr eccentricity pacing
50 during the Miocene, followed by the emergence of stronger 100 kyr and 40 kyr variability later in the Neogene
51 (Holbourn et al., 2007; Tian et al., 2013; Westerhold et al., 2020; Liu et al., 2024).

52 Orbital variation in eccentricity, obliquity, and precession regulate the seasonal and latitudinal distribution of
53 incoming solar radiation, thereby influencing the climate system such as monsoon strength, cryosphere dynamics,
54 and ocean–atmosphere coupling (Berger, 1978; Hays et al., 1976; Milanković, 1941). Specifically, summer
55 insolation in the high latitudes of the Northern Hemisphere (NH) has been suggested as a key driver of Quaternary
56 glacial-interglacial cycle (Milanković, 1941). Elevated NH summer insolation enhances land-sea thermal contrast,
57 shifts convection inland, strengthens rainfall from Africa to Southeast Asia (Battisti et al., 2014; Bosmans et al., 2018;
58 Dai et al., 2024; Herold et al., 2012; Yin et al., 2012). In the Southern Hemisphere, orbital forcing modulates
59 Antarctic ice-sheet sensitivity, with geological records indicating enhanced obliquity responses from the Miocene
60 onwards (Levy et al., 2019; Naish et al., 2009; Van Peer et al., 2024). Eccentricity-paced variations in the marine
61 carbon cycle and tropical hydrological processes further point to a strong imprint of long-period orbital forcing
62 during this interval (Holbourn et al., 2007; Tian et al., 2013; Liu et al., 2024).

63 However, the climate expression of orbital forcing is not stationary through time. Miocene $\delta^{18}\text{O}$ and $\delta^{13}\text{C}$ records are
64 dominated by 400 kyr eccentricity variability, whereas stronger 100 kyr and 40 kyr cycles emerge later in the
65 Neogene (Holbourn et al., 2007; Westerhold et al., 2020). Comparable shifts during the Mid-Pleistocene transition
66 (MPT) and the Mid-Brunhes Transition (MBT) occurred without major changes in orbital parameters, suggesting an
67 important role for background climate state, threshold behavior, or internal feedbacks related to the Southern Ocean

68 ventilation and Antarctic ice dynamics (Kemp et al., 2010; Yin, 2013). Recent analyses further emphasize changes
69 in the relative influence of precession and obliquity across these transitions (Berger et al., 2024). Collectively, these
70 observations imply a state-dependent orbital–climate relationship rather than a simple linear response to insolation
71 forcing.

72 Although geological archives document pervasive orbital pacing during the Miocene, the mechanisms by which
73 orbital-scale insolation variations translate into regional climate responses—particularly in warm climates lacking
74 large Northern Hemisphere ice sheets—remain poorly constrained. Proxy records alone cannot isolate the respective
75 roles of forcing, feedbacks, and internal variability, and climate modeling studies explicitly targeting orbital effects
76 under realistic Miocene boundary conditions remain scarce.

77 Here, we use fully coupled climate model simulations to evaluate the climate response to orbital-driven insolation
78 changes in the Miocene framework. We assess the sensitivity of high-latitude climate, tropical hydrological cycle,
79 and ocean-cryosphere interactions to orbital forcing, and how these responses differ from those under the pre-
80 industrial (PI) condition. By comparing these responses with those patterns inferred from proxy records, we assess
81 how background climate state modulates orbital-scale climate variability and to provide context for evaluation of
82 orbital-climate coupling through the Neogene.

83 **2 Climate model and simulation setup**

84 **2.1 FGOALS-g3 climate model and simulation setup**

85 We use the fully coupled general circulation model FGOALS-g3, which is part of CMIP6. It has been widely
86 applied to both present-day climate studies (Li et al., 2020; Lin et al., 2022; Wang et al., 2020) and paleoclimate
87 simulations from the Miocene to the mid-Holocene (Wei et al., 2023; Zheng et al., 2020). A detailed description of
88 model components and evaluation is provided in the Supplement.

89 Two baseline experiments were conducted: a pre-industrial (PI) simulation and a Miocene simulation (MCO). The
90 PI simulation is performed with standard pre-industrial climate forcing. The MCO simulation adopts the MioMIP2
91 protocol and incorporates reconstructed Miocene boundary conditions, including paleogeography, vegetation, ice
92 sheet, and an atmospheric CO₂ concentration three times the PI level (Burls et al., 2021). The solar constant, orbital
93 parameters, and aerosol concentration in MCO are kept identical to those of the PI simulation.

94 To examine the climate response to orbital forcing, we conducted sensitivity simulations by modifying orbital
95 parameters in each baseline experiment. For both the PI and MCO climate, we performed a “winter-perihelion”
96 simulation with minimum boreal summer insolation (NSI_{min}), and a “summer-perihelion” simulation with
97 maximum boreal summer insolation (NSI_{max}) (Table 1). These orbital simulations are designed to represent mid- to
98 late Miocene intervals characterized by pronounced $\delta^{13}\text{C}$ excursions and widespread carbon burial associated with
99 the Monterey events (Anttila et al., 2023; Holbourn et al., 2018; Westerhold et al., 2020). Specifically, we selected
100 two representative time slices at 10.777 Ma (NSI_{max}) and 10.767 Ma (NSI_{min}) (Fig. S1). This orbital sensitivity

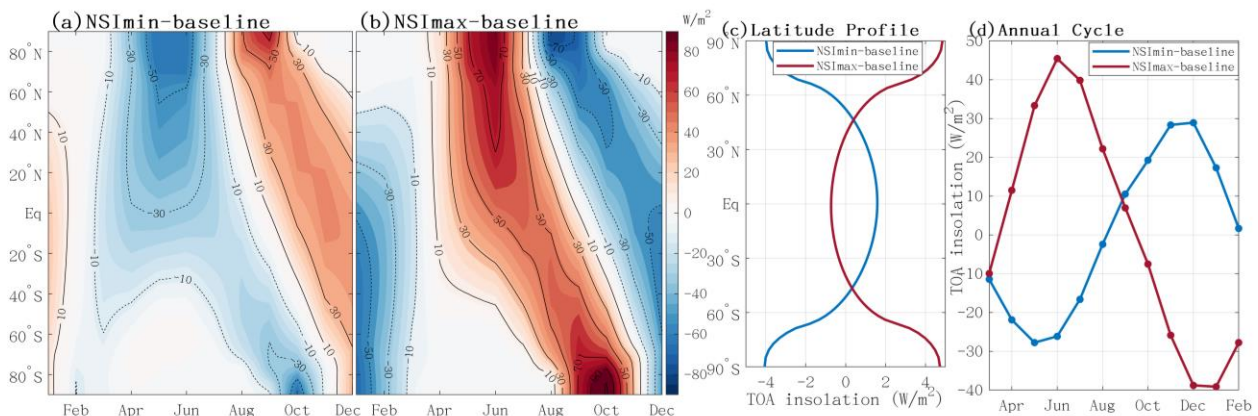
101 framework has been widely applied in previous Pleistocene studies (Battisti et al., 2014; Bosmans et al., 2018; Dai
 102 et al., 2024). Although eccentricity also differs between these configurations, its effect is included in the effect of
 103 precession which amplitude is modulated by eccentricity.

104 **Table 1.** Model simulation setup

Simulation	Geography Setting	pCO ₂ (ppm)	Orbital forcing			Duration of simulation (yrs)	TOA* (W/m ²)	GMAT** (°C)
			Eccentr	Obliquity (rad)	Long. Perih			
PI			0.0167	0.4091	102.040°	1700	-0.04	15.61
PINSImax	Modern	280	0.0508	0.4208	281.387°	300	0.05	15.75
PINSImin			0.0599	0.3983	68.158°	300	-0.17	15.71
MCO			0.0167	0.4091	102.040°	1700	0.34	22.32
MCONSImax	Miocene	840	0.0508	0.4208	281.387°	400	0.28	22.47
MCONSImin	(~15Ma)		0.0599	0.3983	68.158°	400	0.30	22.58
MCO_1x		280	0.0167	0.4091	102.040°	1000	0.15	22.58

105 TOA*: Top-of-Atmosphere (TOA) radiation imbalance; GMAT**: Global Mean Air Temperature.
 106
 107

108 The June insolation contrast between NSImax and NSImin is substantial, reaching 130 W/m² at 65°N and 90 W/m²
 109 at 20°N (Fig. 1, S1 & S2). These seasonal insolation anomalies primarily result from differences in the longitude of
 110 perihelion (281° and 68°), corresponding to boreal summer and winter occurring near perihelion, respectively (Fig.
 111 S1 & Table 1). In NSImax, enhanced boreal summer insolation and reduced winter insolation amplify the globally
 112 averaged annual insolation cycle by ~80 W/m² relative to the baseline, whereas NSImin weakens the annual cycle
 113 by 60 W/m² (Fig. 1d). Meridionally, NSImax increases annual-mean insolation at high latitudes while slightly
 114 reducing it in the tropics due to its higher obliquity, with the opposite pattern in NSImin (Fig. 1c). Applying these
 115 orbital forcings yields two pairs of experiments: PINSImax/PINSImin for the pre-industrial and
 116 MCONSImax/MCONSIminAI for the Miocene. It's worth to note that although these specific configurations are
 117 chosen for the Miocene, similar orbital patterns recur throughout the Pleistocene (Fig. S3).



118

119 **Figure 1. Orbital-induced insolation changes (W/m^2) of the NSImin (a) and NSImax (b) simulations from the baseline**
120 **simulation, and their latitude profile of annual-mean insolation (c) and globally averaged annual insolation cycle (d).**

121 Both PI and MCO baseline simulations were each run for 1700 years to reach quasi-equilibrium. The orbital
122 simulations were then branched from the year 1601th of the corresponding baseline runs and integrated for additional
123 300 (PINSImax, PINSImin) and 400 years (MCONSImax, MCONSImin), respectively. Over the final 100 years of
124 each experiment, the global mean top-of-Atmosphere (TOA) radiation imbalance within $\pm 0.34 \text{ W/m}^2$ (Table. 1).

125 We note that the MCO runs have not fully reached quasi-equilibrium. However, as this study focuses primarily on
126 the atmospheric and upper-ocean response, the remaining drift does not affect the interpretation of the results.
127 Monthly means from these equilibrated periods are used for all subsequent analysis. The PI simulation reasonably
128 captures the spatial pattern and magnitude of present-day seasonal temperature variations relative to the CMIP5
129 multi-model mean and ERA5, with a minor cold bias in Arctic Eurasia linked to excessive sea ice (see SI for more
130 details).

131 **2.2 Diagnostic analysis**

132 To diagnose the processes controlling the temperature response to orbital forcing, we apply a one-dimensional
133 Energy Balance Model analysis (EBM) following (Heinemann et al., 2009; Wei et al., 2023). The EBM balances
134 net incoming shortwave radiation against outgoing longwave radiation and meridional heat transport, using radiative
135 fluxes from the coupled general circulation model (GCM) as input. Temperature differences between simulations are
136 decomposed into contributions from surface albedo, water-vapor greenhouse trapping, cloud radiative effects, and
137 meridional heat transport. Cloud effects are further decomposed into shortwave and longwave components.

138 The EBM components reproduce the zonal-mean temperature responses simulated by the GCM, with deviations
139 generally within $0.1\text{-}0.9 \text{ }^\circ\text{C}$ (Fig. S4). Slight underestimates occur in the NH subtropics and polar regions, while
140 overestimation appears near $70\text{-}80 \text{ }^\circ\text{N}$ (Fig. S4), consistent with previous studies and mainly reflecting nonlinear
141 processes associated with seasonal and zonal averaging (Lunt et al., 2012). The EBM decomposition is used to
142 interpret the relative roles of albedo, water vapour, clouds, and heat transport in shaping the spatial structure of
143 orbital-scale temperature changes.

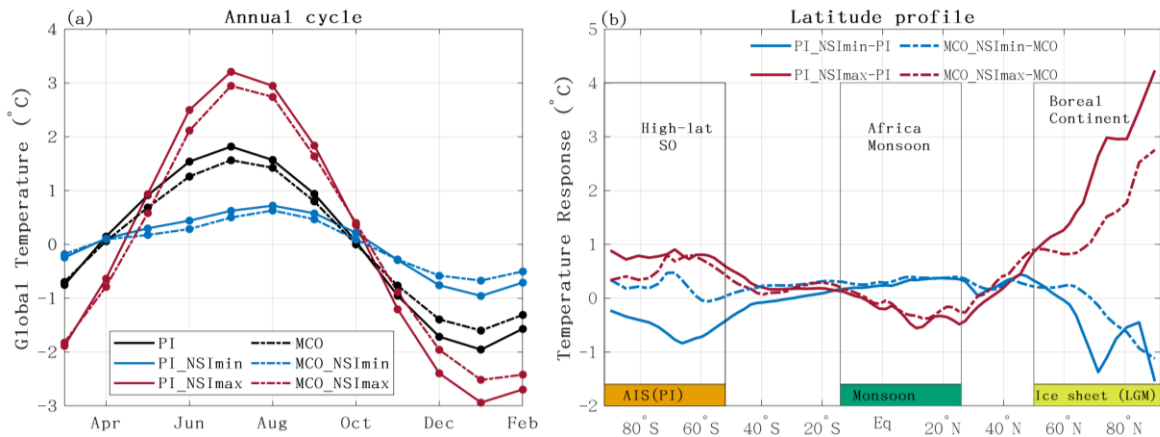
144 **3 Results and Discussion**

145 **3.1 Weaker seasonality of temperature response during the Miocene**

146 The annual temperature cycle in the MCO is $3.2 \text{ }^\circ\text{C}$, smaller than the $3.7 \text{ }^\circ\text{C}$ in PI, reflecting reduced July warming and
147 weaker January cooling (Fig 2a). The MCO-1x simulation shows an intermediate amplitude of $\sim 3.5 \text{ }^\circ\text{C}$ (Fig. S5),
148 suggesting both elevated CO_2 and Miocene boundary conditions contribute to the reduced seasonality, with the latter
149 exerting a slightly larger influence.

150 Orbital forcing substantially modulates the amplitude of the seasonal temperature cycle. Reduced boreal summer
151 insolation weakens the seasonal cycle by 1.9 to $1.3 \text{ }^\circ\text{C}$ in MCONSImin, and by $2.$ to $1.6 \text{ }^\circ\text{C}$ in PI_NSImin. Conversely,

152 increased boreal summer insolation intensifies seasonality, raising it to 5.4 °C in MCONSI_{max} and 6.4 °C in
 153 PI_{NSI_{max}} (Fig. 2). Consequently, seasonal global-mean air temperature (GMAT) variations rise by more than 2 °C
 154 in the NSI_{max} simulations and decline by a similar magnitude in the NSI_{min} simulations relative to their respective
 155 baselines. The JJA temperature differences between NSI_{max} and NSI_{min} exceed 2.5 °C (Fig. 2), comparable to the
 156 ~3 °C global cooling during the late Miocene (Westerhold et al., 2020), underscoring the potential of orbital forcing
 157 to generate large-amplitude temperature variability.



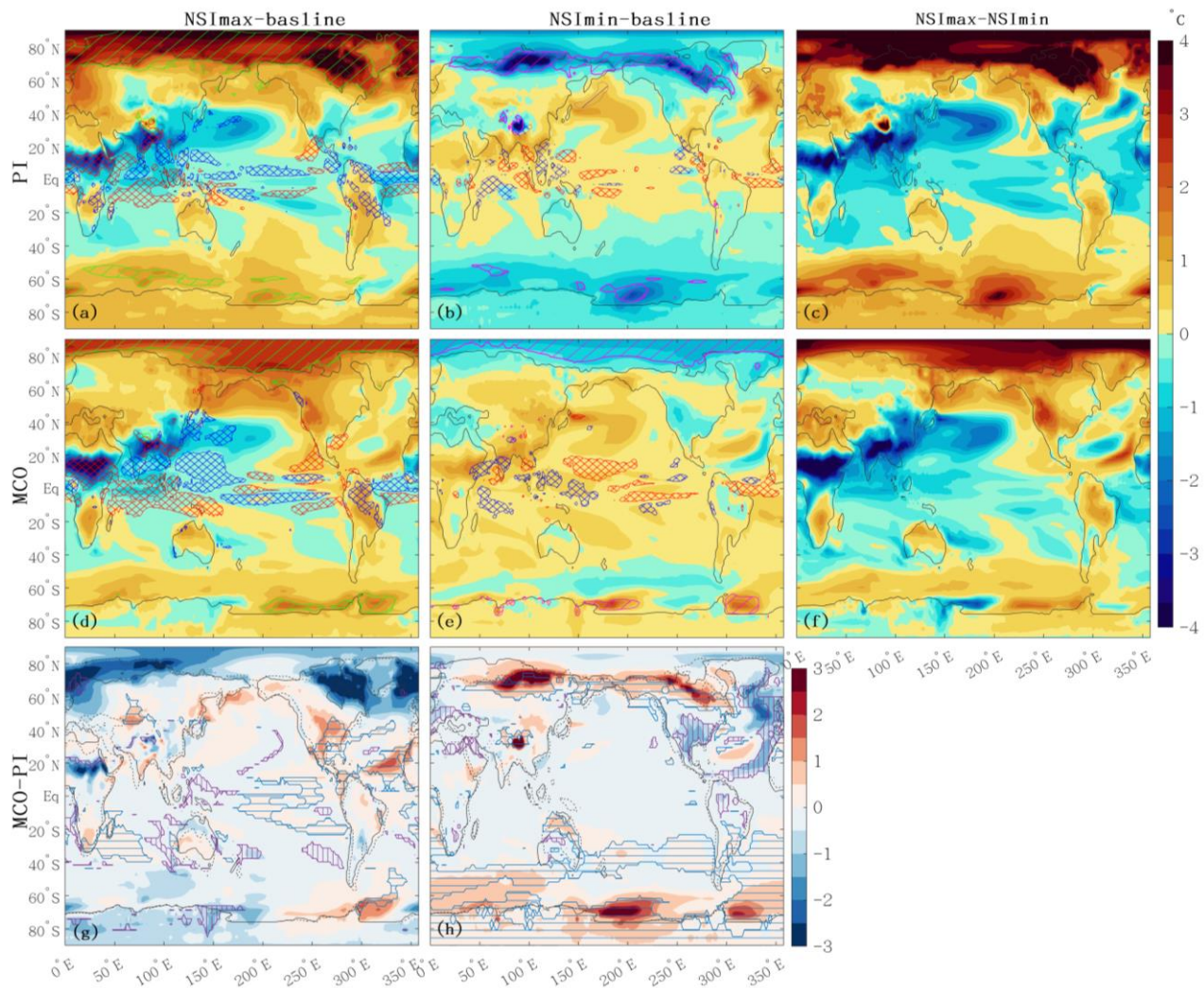
158

159 **Figure 2. (a) Annual cycle of temperature anomalies relative to the annual mean, with black, red and blue lines**
 160 **representing baseline, NSI_{max} and NSI_{min} simulations, respectively. Solid lines denote the PI climate, and dashed lines**
 161 **denote the Miocene climate. (b) Latitude profile of temperature response to orbital forcing, shown as anomalies to their**
 162 **baseline simulation and using the same color scheme as in (a). The locations of modern Antarctic Ice sheet (AIS), major**
 163 **monsoon regions and the Last glacial maximum Ice sheets are indicated in (b).**

164 Compared with the PI climate, the MCO simulation exhibits weaker seasonality and a dampened orbital response
 165 (Fig. 2a). The GMAT response to orbital forcing is diminished by ~0.1 °C in both MCONSI_{min} and MCONSI_{max}
 166 simulations, yielding ~10 % weaker changes in seasonal amplitude. This diminished Miocene temperature response
 167 is also evident in the latitudinal profile, showing differences of up to 1 °C at high latitudes (Fig. 2b). Because
 168 comparable analyses are not yet available for other warm climate intervals, it remains uncertain whether the
 169 reduced orbital response identified here is specific to the MCO or reflect a more general feature of warm climate
 170 states. This question requires further investigation. A detailed analysis of the ocean circulation response will be
 171 presented in a separate study focusing on Miocene ocean–atmosphere dynamics. This reduced Miocene seasonality is
 172 consistent with proxy evidence indicating weaker seasonality in Europe during the warming Miocene (Harzhauser et
 173 al., 2011), and a reduced meridional temperature gradient in North America (Reichgelt et al., 2023). Variation in
 174 Miocene seasonal response to identical orbital forcing can alter the relationship between growing-season and annual
 175 mean temperatures, potentially biasing proxy-based temperature reconstructions. This highlight the importance of
 176 applying seasonality adjustments that account for different paleoclimate background, rather than relying solely on
 177 modern analogues, when addressing well-documented seasonal biases in proxies (Bova et al., 2021; Marsicek et al.,
 178 2018; Laepple and Lohmann, 2009; Laepple et al., 2022)..

179 **3.2 Spatially varied Miocene temperature responses**

180 The NSI_{max} and NSI_{min} simulations show overall anti-phased annual mean temperature responses (Fig. 3).
 181 Compared to the MCO and PI baselines, NSI_{max} simulations show a dipole pattern, with polar warming but cooling
 182 in the tropics and subtropics of both hemispheres. Conversely, NSI_{min} simulations show high-latitude cooling and
 183 extratropical and tropical warming that extending up to ~60°N and 40°S. Similar high versus low- latitude contrasts
 184 have been reported in simulations of interglacials characterized by high obliquity and precession, such as Mid-
 185 Holocene (Brierley et al., 2020; Dai et al., 2024) and other interglacials (Yin et al., 2012; Herold et al., 2012). These
 186 patterns are primarily related to the change in obliquity and precession, and are further amplified by feedback
 187 including high-latitude albedo changes and shifts in the tropical hydrological cycle (Fig. S7 & S8).
 188



189

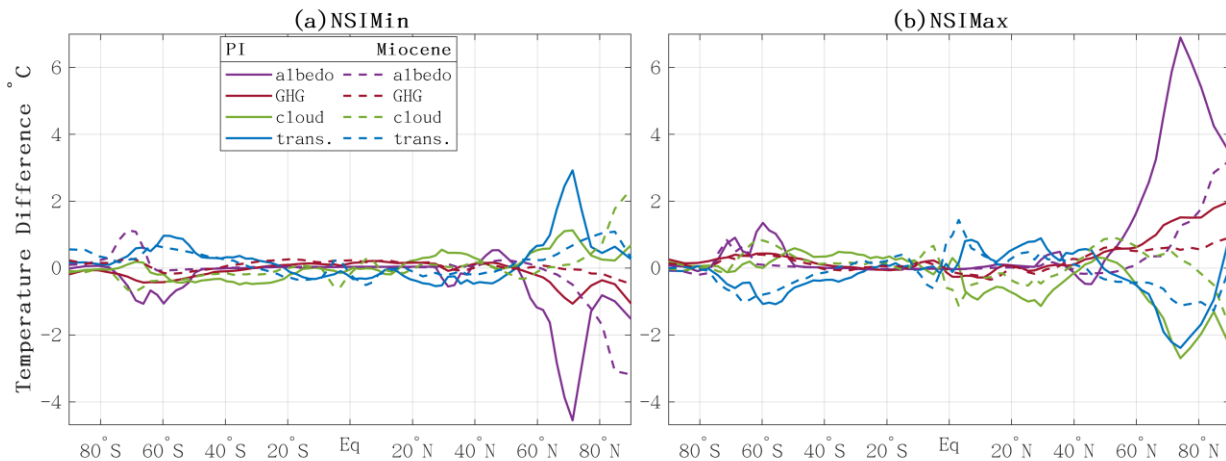
190 **Figure 3. Annual-mean air temperature response (°C).** Upper panel: Anomalies of NSI_{max} and NSI_{min}
 191 simulations relative to the baseline simulation (a, b) and the difference between NSI_{max} and NSI_{min}
 192 (c), all for the PI. Cross marked regions indicate where precipitation increased (red) or decreased (blue) by more
 193 than 0.6 mm/day. Hatching indicates regions where albedo increase (magenta) or decrease (green) by over 5%.

194 Middle panel: Same as upper panel but for the Miocene. Lower panel: Differences between the Miocene and PI
 195 baseline simulations for the NSI_{max} (g) and for the NSI_{min} (h). Blue horizontal and purple vertical hatching regions
 196 indicate where the sign of anomalies is reversed—shifting from negative in PI to positive in Miocene, and vice
 197 versa.

198 3.2.1 Reduced High-latitude Orbital Response in the MCO

199 Compared to PI, the Miocene orbital response is notably weaker at high northern latitudes (Fig. 3). Under PI
 200 conditions, the strongest PINSI_{max} warming (~4.8 °C) occurs over northeast Canada and the Labrador Sea, whereas
 201 the MCONSI_{max} warming is less than half as large (Fig. 3b). Similarly, cooling in the PINSI_{min} simulation reaches
 202 ~4.4 °C over Western Siberia, but only ~1 °C in MCONSI_{min} (Fig. 3a, 3c). The strongest Miocene response —2.8°C
 203 over the Chukchi Sea—remains weaker than its PI counterpart.

204 EBM results show that much of the weaker Miocene temperature responses in NH high-latitudes can be attributed to
 205 smaller changes in surface albedo (Fig. 4). In the Miocene, the albedo contribution is roughly half of that in the PI.
 206 For example, albedo-driven warming reaches ~6 °C in PINSI_{max} but only ~3 °C in MINSI_{max}. Similarly,
 207 MCONSI_{min} shows poleward-shifted and weaker albedo-driven cooling than PINSI_{min}. This reduced albedo
 208 feedback dampens the Miocene temperature responses to orbital forcing, with temperature changes closely matching
 209 the spatial pattern of the Miocene albedo response (Fig. 3). Further analysis (Fig. S7) shows that strong albedo
 210 changes in the PI simulations coincides with ice sheets and sea ice, where ice–albedo feedbacks amplifies the
 211 climate response to orbital forcing. By contrast, the warmer Miocene climate, characterized by widespread
 212 vegetation, limited sea ice, and lower surface albedo, is less sensitive to orbital perturbations.



213

214 **Figure 4. Zonal mean surface temperature responses to orbital forcing from the EBM decomposition.** Total response is
 215 decomposed into contributions from the surface albedo (albedo), water vapor’s greenhouse (GHG), meridional heat transport
 216 (trans), and cloud effects (cloud).

217 The strong albedo response is further reinforced by water-vapor greenhouse effect but partly offset by cloud
 218 changes. Water-vapor contributions largely follow albedo patterns, reflecting their dependence on surface energy
 219 availability, whereas clouds exert an opposing influence. Further decomposition into shortwave and longwave

220 components reveal that shortwave cloud radiative effects dominate, yielding a generally weaker net negative
221 feedback in the Miocene (Fig. S4).

222 These results are consistent with previous studies suggesting a reduced meridional temperature gradient in eastern
223 North America during the warm Miocene relative to the modern era (Reichgelt et al., 2023). The larger temperature
224 variations in the PI simulation point to enhanced sensitivity to orbital forcing, consistent with the development of
225 pronounced NH glacial-interglacial cycles. In contrast, the Miocene's dampened response implies weakened
226 temperature response to orbital forcing and thus possibly reduced amplitude of orbital-scale climate variability under
227 warmer background conditions.

228 **3.2.2 Enhanced tropical North Africa cooling in the MCONSI_{max}**

229 An exception to the weaker Miocene response is the enhanced tropical North Africa cooling in the MCONSI_{max}
230 simulation (Fig. 3d). Here, annual-mean temperature decreases by 4.4 °C—greater than the 3.8 °C in PINSI_{max}—
231 and the anomaly extends farther north. Seasonal decomposition indicates that this cooling persists even during
232 boreal summer, despite increased insolation (Fig. S1 & S8). It coincides with intensified precipitation, indicating a
233 dominant role of hydrological changes in controlling temperature.

234 These enhanced Miocene cooling effects under MCONSI_{max} are consistent with increased precipitation. EBM
235 diagnostics further reveal a stronger cooling contribution from water-vapor and cloud in Miocene (-0.34 and -
236 1.12°C), in contrast to warming contributions in PI (0.28 and 0.94°C). Additional analysis of moisture flux
237 divergence suggests that more moisture is from the Tethys Sea during the Miocene, feeding precipitation over
238 tropical North Africa (Fig. S9). A wider Tethys Sea provides an efficient moisture source, while a warmer climate
239 accelerates the hydrological cycle (Fig. S8) (Sarr et al., 2022; Huntington, 2006). These findings are in line with
240 proxy evidence for intensified Miocene hydrological cycle and increased precipitation over the Mediterranean and
241 North African region (Hoelzmann et al., 2001; Liu et al., 2024; Acosta et al., 2024; Zhang et al., 2014), supporting
242 the interpretation that the cooling in MCONSI_{max} is associated with enhanced hydrological feedbacks.

243 **3.2.3 Disrupted Southern Ocean warming in the MCONSI_{min}**

244 In MCONSI_{min} simulation, unexpected warming occurs over the Ross and Weddell Sea despite reduced local
245 annual-mean insolation, in contrast to the cooling simulated in PINSI_{min}. This Miocene response deviates from the
246 near-symmetric responses observed in PI, which broadly follows local insolation changes.

247 This anomalous warming is particularly evident during Austral winter (Fig. S11), disrupting the expected anti-phase
248 signal and generating an out-of-phase response. EBM analysis indicates that the reversed temperature response in
249 MCONSI_{min} (1.1°C warming at 71 °S instead of cooling) is mainly attributed to albedo and water-vapor effects
250 (Fig. 4). During the Miocene, the maximum sea-ice edge lies closer to the pole (~70°S), where significant winter
251 insolation anomalies (Fig. S10) promote positive ice-albedo feedback: reducing sea ice and enhanced ocean-
252 atmosphere heat exchange, and additional atmospheric water vapor (Fig. 3 & S11). In contrast, PI sea ice extends to
253 lower latitudes, where insolation changes were smaller, limiting sensitivity to seasonal orbital forcing (Fig. S11). It

254 is worth noting that land ice-sheet is prescribed in the model and therefore exerts a one-way influence on the climate
255 system; associated feedback would like amplify the response. A full assessment of this effect, however, would
256 require coupling with an interactive ice-sheet model (Halberstadt et al., 2021).

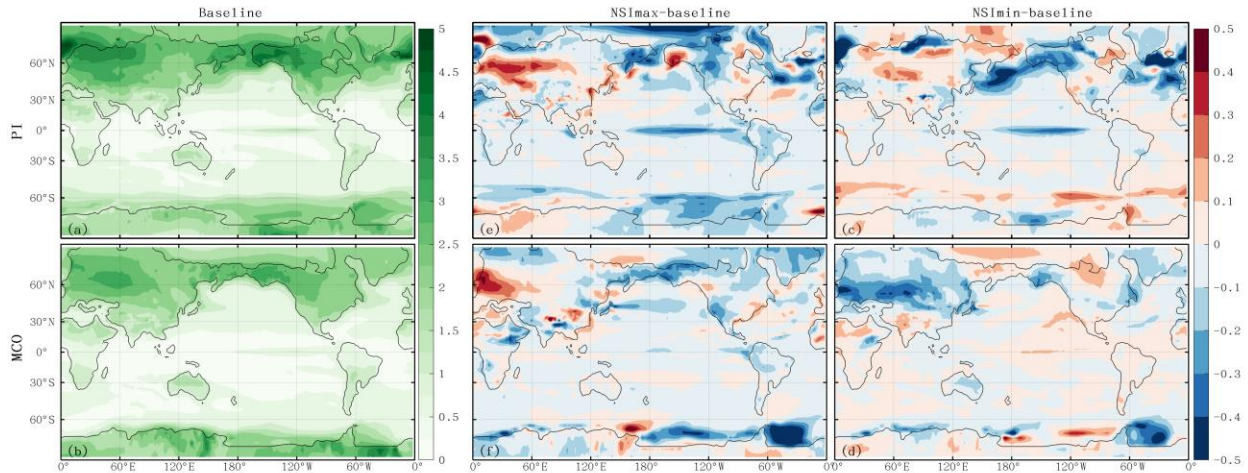
257 These results support geological evidence that ocean-atmosphere-ice sheet interactions amplified Antarctic ice-
258 sheets sensitivity to orbital forcing during Miocene ice-sheet growth (De Vleeschouwer et al., 2017; Levy et al.,
259 2019; Naish et al., 2009). Sediment records further indicate a stronger and more stable climate response as ice sheets
260 and sea ice expanded, compared with warmer periods such as the Early Eocene, when carbon-climate coupling
261 dominated (De Vleeschouwer et al., 2017; Levy et al., 2019; Naish et al., 2009; Reichgelt et al., 2023; Setty et al.,
262 2023). Overall, these findings underscore strong background-state control on Southern Ocean sea-ice feedbacks
263 (Bloch - Johnson et al., 2021).

264 **3.3 Spatially diverse Miocene responses to orbital forcing and weakened internal temperature variability**

265 Beyond differences in magnitude, the spatial extent of warming and cooling response also differs between the PI and
266 Miocene simulation. Under PI conditions, high-latitude temperature responses are largely symmetric between
267 NSImax and NSImin. In contrast, the Miocene simulations show warming in both MCONSImin and MCONSImax
268 over Siberia and Alaska, resulting in distinct regional responses across 60-70 °N spanning Eurasia, Alaska and North
269 America continent (Fig. 3e, blue line). Similarly, the Weddell Sea and Ross Sea exhibit overall warming in both
270 Miocene orbital simulations, deviating from the symmetric PI behavior (Fig. 3 & S11). These deviations suggest a
271 less symmetric and less predictable Miocene response, likely consistent with proxy evidence for dominance of
272 longer-period orbital variability (e.g. the 400-kyr) rather than 40 kyr and 100 kyr cycle characteristic of the
273 Pleistocene [Holbourn et al., 2007; Tian et al., 2013; Westerhold et al., 2020; Liu et al., 2024]. This also implies that
274 simple NSImax minus NSImin, without examining spatial patterns in detail, can obscure nonlinear responses—
275 particularly under warmer background conditions.

276 In addition to mean changes, internal temperature variability provides insight into climate stability (Harzhauser et
277 al., 2011). We therefore examine de-seasonalised variability (standard deviation) over key high-latitude regions of
278 active glacial dynamics. Mid-latitude Eurasia and North America exhibit higher variability in the PI simulation,
279 which is further amplified in both PINSImin and PINSImax, reflecting enhanced ice-albedo interactions. By
280 contrast, Miocene variability is lower and further reduced in MCONSImin (Fig. 5), suggesting a more stable high-
281 latitude climate with dampened feedbacks under warmer conditions. Reduced eastern Pacific variability in the
282 Miocene likely reflects enhanced inter-basin exchange through an open Panama Seaway, which buffers regional
283 responses (Lunt et al., 2008). The stronger PI variability supports pronounced NH glacial-interglacial cycles,
284 whereas the dampened Miocene response suggests weaker orbital pacing.

285



286

287 **Figure 5. Standard deviation of deseasonalized temperature, and its responses to orbital forcing.**

288 **4 Conclusions and Implications**

289 The Miocene, particularly the interval following the Miocene Climatic Optimum (MCO), shows strong orbital
 290 pacing in geological records despite warm boundary conditions, limited Northern Hemisphere ice, and reduced
 291 meridional temperature gradients. However, the mechanisms linking orbital forcing to climate variability during this
 292 warm epoch are not well understood. By conducting parallel orbital sensitivity experiments under mid-Miocene and
 293 pre-industrial (PI) conditions, we evaluate how background climate state modulates the expression of orbital-driven
 294 temperature change.

295 In general, both temperature exhibit broadly anti-phased temperature responses between maximum and minimum
 296 boreal summer insolation, each characterized by a meridional high-to-low latitude dipole. However, the Miocene
 297 response is $\sim 1^\circ\text{C}$ weaker, with regionally dependent contrasts and reduced symmetry between two orbital cases.
 298 Three key differences emerge: (1) reduced Northern Hemisphere continental sensitivity in the Miocene, reflecting
 299 weaker surface-albedo, water-vapor, and cloud radiative effects in a warmer, low-ice, vegetation-modified climate—
 300 consistent with proxy evidence for diminished high-latitude climate sensitivity after the MCO; (2) stronger
 301 hydrological cooling in North Tropical Africa in MCONSI_{max}, driven by enhanced precipitation, cloud, and
 302 moisture-feedbacks within an intensified Miocene hydrological cycle supported by a wider Tethys Sea —indicating
 303 amplified hydrological sensitivity to orbital forcing in warm climates; and (3) a reversed Southern Ocean warming
 304 in MCONSI_{min} under lower insolation, where poleward-restricted Miocene sea ice allows winter insolation
 305 anomalies to trigger positive ice-albedo feedbacks, matching proxy evidence for heightened Antarctic obliquity
 306 sensitivity.

307 These differences highlight that the strength and pattern of orbital impact depend strongly on background climate
 308 state. The Miocene’s weaker seasonal amplitude and reduced internal variability imply diminished orbital pacing
 309 relative to the PI climate, consistent with dominant 400-kyr eccentricity variability in Miocene proxy records. This

310 has two key implications: first, Miocene proxy reconstructions may overestimate annual mean temperatures if
311 modern seasonal analogues are applied, underscoring the need for context-specific seasonality corrections; and
312 second, the stronger and more symmetric PI response reflects the emergence of high-latitude cryosphere feedbacks
313 central to Quaternary glacial–interglacial cycles.

314

315 **Acknowledgments**

316 The authors are grateful to the two anonymous referees for their valuable comments that substantially improved the
317 manuscript, as well as the Editor, Ran Feng, for managing the review process. This study was supported by the
318 National Key R&D program of China (2023YFF0803902) and (2023YFF0803904). We appreciate the technical
319 support of the National Large Scientific and Technological Infrastructure, *Earth System Numerical Simulation*
320 *Facility* (<https://estr.cn/31134.02.EL>).

321

322 **Open Research**

323 Model output data from this study are available at Zhang (2025).

324

325 **Author contributions**

326 Conceptualization & Study Design: YZ;

327 Methodology & Simulations: YZ, JW, with support from WZ;

328 Formal Analysis & Investigation: YZ, with guidance from YQ, A. de B., ZS, LZ;

329 Data Curation: ZL, ND;

330 Writing – Original Draft: YZ;

331 Writing – Review & Editing: All authors.

332

333 **Competing interests**

334 Some authors are members of the editorial board of journal *Climate of the Past*.

335

336 **References**

337 Acosta, R. P., Burls, N. J., Pound, M. J., Bradshaw, C. D., De Boer, A. M., Herold, N., Huber, M., Liu, X., Donnadieu,
338 Y., Farnsworth, A., Frigola, A., Lunt, D. J., von der Heydt, A. S., Hutchinson, D. K., Knorr, G., Lohmann, G.,

339 Marzocchi, A., Prange, M., Sarr, A. C., Li, X., and Zhang, Z.: A Model-Data Comparison of the Hydrological
340 Response to Miocene Warmth: Leveraging the MioMIP1 Opportunistic Multi-Model Ensemble,
341 *Paleoceanography and Paleoclimatology*, 39, e2023PA004726, <https://doi.org/10.1029/2023PA004726>, 2024.
342 Battisti, D. S., Ding, Q., and Roe, G. H.: Coherent pan-Asian climatic and isotopic response to orbital forcing of
343 tropical insolation, *Journal of Geophysical Research: Atmospheres*, 119, 10.1002/2014jd021960, 2014.
344 Berger: Long-Term Variations of Daily Insolation and Quaternary Climatic Changes %J *Journal of Atmospheric*
345 *Sciences*, 35, 2362-2367, [https://doi.org/10.1175/1520-0469\(1978\)035<2362:LTVODI>2.0.CO;2](https://doi.org/10.1175/1520-0469(1978)035<2362:LTVODI>2.0.CO;2), 1978.
346 Berger, Yin, Q., and Wu, Z.: Length of astronomical seasons, total and average insolation over seasons,
347 *Quaternary Science Reviews*, 334, 108620, <https://doi.org/10.1016/j.quascirev.2024.108620>, 2024.
348 Bloch-Johnson, J., Rugenstein, M., Stolpe, M. B., Rohrschneider, T., Zheng, Y., and Gregory, J. M.: Climate
349 Sensitivity Increases Under Higher CO2 Levels Due to Feedback Temperature Dependence, *Geophysical*
350 *Research Letters*, 48, 10.1029/2020gl089074, 2021.
351 Bosmans, J. H. C., Erb, M. P., Dolan, A. M., Drijfhout, S. S., Tuentner, E., Hilgen, F. J., Edge, D., Pope, J. O., and
352 Lourens, L. J.: Response of the Asian summer monsoons to idealized precession and obliquity forcing in a set
353 of GCMs, *Quaternary Science Reviews*, 188, 121-135, 10.1016/j.quascirev.2018.03.025, 2018.
354 Bova, S., Rosenthal, Y., Liu, Z., Godad, S. P., and Yan, M.: Seasonal origin of the thermal maxima at the Holocene
355 and the last interglacial, *Nature*, 589, 548-553, 10.1038/s41586-020-03155-x, 2021.
356 Brierley, C. M., Zhao, A., Harrison, S. P., Braconnot, P., Williams, C. J. R., Thornalley, D. J. R., Shi, X., Peterschmitt,
357 J.-Y., Ohgaito, R., Kaufman, D. S., Kageyama, M., Hargreaves, J. C., Erb, M. P., Emile-Geay, J., D'Agostino, R.,
358 Chandan, D., Carré, M., Bartlein, P. J., Zheng, W., Zhang, Z., Zhang, Q., Yang, H., Volodin, E. M., Tomas, R. A.,
359 Routson, C., Peltier, W. R., Otto-Bliesner, B., Morozova, P. A., McKay, N. P., Lohmann, G., Legrande, A. N., Guo,
360 C., Cao, J., Brady, E., Annan, J. D., and Abe-Ouchi, A.: Large-scale features and evaluation of the PMIP4-CMIP6
361 midHolocene simulations, *Climate of the Past*, 16, 1847-1872, 10.5194/cp-16-1847-2020, 2020.
362 Burls, N. J., Bradshaw, C. D., De Boer, A. M., Herold, N., Huber, M., Pound, M., Donnadieu, Y., Farnsworth, A.,
363 Frigola, A., Gasson, E., von der Heydt, A. S., Hutchinson, D. K., Knorr, G., Lawrence, K. T., Lear, C. H., Li, X.,
364 Lohmann, G., Lunt, D. J., Marzocchi, A., Prange, M., Riihimaki, C. A., Sarr, A. C., Siler, N., and Zhang, Z.: Simulating
365 Miocene Warmth: Insights From an Opportunistic Multi-Model Ensemble (MioMIP1), *Paleoceanography and*
366 *Paleoclimatology*, 36, 10.1029/2020pa004054, 2021.
367 Dai, G., Zhang, Z., Otterå, O. H., Langebroek, P. M., Yan, Q., Zhang, R., and Zhu, Z.: Winter Insolation Modulates
368 Boreal Tropical Monsoonal Temperatures in the Late Pleistocene, *Journal of Geophysical Research:*
369 *Atmospheres*, 129, 10.1029/2023jd040577, 2024.
370 De Vleeschouwer, D., Vahlenkamp, M., Crucifix, M., and Pälike, H.: Alternating Southern and Northern
371 Hemisphere climate response to astronomical forcing during the past 35 m.y, *Geology*, 45, 375-378,
372 10.1130/g38663.1, 2017.
373 Frigola, A., Prange, M., and Schulz, M.: A dynamic ocean driven by changes in CO2 and Antarctic ice-sheet in
374 the middle Miocene, *Palaeogeography, Palaeoclimatology, Palaeoecology*, 579, 110591,
375 <https://doi.org/10.1016/j.palaeo.2021.110591>, 2021.
376 Goldner, A., Herold, N., and Huber, M.: The challenge of simulating the warmth of the mid-Miocene climatic
377 optimum in CESM1, *Clim. Past*, 10, 523-536, 10.5194/cp-10-523-2014, 2014.
378 Halberstadt, A. R. W., Chorley, H., Levy, R. H., Naish, T., DeConto, R. M., Gasson, E., and Kowalewski, D. E.: CO2
379 and tectonic controls on Antarctic climate and ice-sheet evolution in the mid-Miocene, *Earth and Planetary*
380 *Science Letters*, 564, 116908, <https://doi.org/10.1016/j.epsl.2021.116908>, 2021.
381 Harzhauser, M., Piller, W. E., Müllegger, S., Grunert, P., and Micheels, A.: Changing seasonality patterns in
382 Central Europe from Miocene Climate Optimum to Miocene Climate Transition deduced from the *Crassostrea*
383 isotope archive, *Global and Planetary Change*, 76, 77-84, 10.1016/j.gloplacha.2010.12.003, 2011.
384 Hays, J. D., Imbrie, J., and Shackleton, N. J.: Variations in the Earth's Orbit: Pacemaker of the Ice Ages, 194,
385 1121-1132, doi:10.1126/science.194.4270.1121, 1976.

386 Heinemann, M., Jungclaus, J. H., and Marotzke, J.: Warm Paleocene/Eocene climate as simulated in
387 ECHAM5/MPI-OM, *Clim. Past*, 5, 785-802, 10.5194/cp-5-785-2009, 2009.

388 Herold, N., Yin, Q. Z., Karami, M. P., and Berger, A.: Modelling the climatic diversity of the warm interglacials,
389 *Quaternary Science Reviews*, 56, 126-141, <https://doi.org/10.1016/j.quascirev.2012.08.020>, 2012.

390 Hoelzmann, P., Keding, B., Berke, H., Kröpelin, S., and Kruse, H.-J.: Environmental change and archaeology: lake
391 evolution and human occupation in the Eastern Sahara during the Holocene, *Palaeogeography,*
392 *Palaeoclimatology, Palaeoecology*, 169, 193-217, [https://doi.org/10.1016/S0031-0182\(01\)00211-5](https://doi.org/10.1016/S0031-0182(01)00211-5), 2001.

393 Holbourn, A., Kuhnt, W., Clemens, S., Prell, W., and Andersen, N.: Middle to late Miocene stepwise climate
394 cooling: Evidence from a high-resolution deep water isotope curve spanning 8 million years,
395 *Paleoceanography*, 28, 688-699, 10.1002/2013pa002538, 2013.

396 Holbourn, A., Kuhnt, W., Schulz, M., Flores, J.-A., and Andersen, N.: Orbitally-paced climate evolution during
397 the middle Miocene "Monterey" carbon-isotope excursion, *Earth and Planetary Science Letters*, 261, 534-550,
398 10.1016/j.epsl.2007.07.026, 2007.

399 Holbourn, A., Kuhnt, W., Clemens, S. C., Kochhann, K. G. D., Johnck, J., Lubbers, J., and Andersen, N.: Late
400 Miocene climate cooling and intensification of southeast Asian winter monsoon, *Nat Commun*, 9, 1584,
401 10.1038/s41467-018-03950-1, 2018.

402 Huntington, T. G.: Evidence for intensification of the global water cycle: Review and synthesis, *Journal of*
403 *Hydrology*, 319, 83-95, <https://doi.org/10.1016/j.jhydrol.2005.07.003>, 2006.

404 Kemp, A. E. S., Grigorov, I., Pearce, R. B., and Naveira Garabato, A. C.: Migration of the Antarctic Polar Front
405 through the mid-Pleistocene transition: evidence and climatic implications, *Quaternary Science Reviews*, 29,
406 1993-2009, <https://doi.org/10.1016/j.quascirev.2010.04.027>, 2010.

407 Laepple and Lohmann, G.: Seasonal cycle as template for climate variability on astronomical timescales,
408 *Paleoceanography*, 24, 10.1029/2008pa001674, 2009.

409 Laepple, Shakun, J., He, F., and Marcott, S.: Concerns of assuming linearity in the reconstruction of thermal
410 maxima, *Nature*, 607, E12-E14, 10.1038/s41586-022-04831-w, 2022.

411 Levy, R. H., Meyers, S. R., Naish, T. R., Golledge, N. R., McKay, R. M., Crampton, J. S., DeConto, R. M., De Santis,
412 L., Florindo, F., Gasson, E. G. W., Harwood, D. M., Luyendyk, B. P., Powell, R. D., Clowes, C., and Kulhanek, D. K.:
413 Antarctic ice-sheet sensitivity to obliquity forcing enhanced through ocean connections, *Nature Geoscience*,
414 12, 132-137, 10.1038/s41561-018-0284-4, 2019.

415 Li, L. Y., Yongqiang, Tang, Y., Lin, P., Xie, J., Song, M., Dong, L., Zhou, T., Liu, L., Wang, L., Pu, Y., Chen, X., Chen,
416 L., Xie, Z., Liu, H., Zhang, L., Huang, X., Feng, T., Zheng, W., Xia, K., Liu, H., Liu, J., Wang, Y., Wang, L., Jia, B., Xie,
417 F., Wang, B., Zhao, S., Yu, Z., Zhao, B., and Wei, J.: The Flexible Global Ocean-Atmosphere-Land System Model
418 Grid-Point Version 3 (FGOALS-g3): Description and Evaluation, *Journal of Advances in Modeling Earth Systems*,
419 12, 10.1029/2019ms002012, 2020.

420 Lin, P., Zhao, B., Wei, J., Liu, H., Zhang, W., Chen, X., Jiang, J., Ding, M., Man, W., Jiang, J., Zhang, X., Ding, Y.,
421 Bai, W., Jin, C., Yu, Z., Li, Y., Zheng, W., and Zhou, T.: The Super-large Ensemble Experiments of CAS FGOALS-
422 g3, *Advances in Atmospheric Sciences*, 39, 1746-1765, 10.1007/s00376-022-1439-1, 2022.

423 Liu, F., Du, J., Huang, E., Ma, W., Ma, X., Lourens, L. J., and Tian, J.: Accelerated marine carbon cycling forced by
424 tectonic degassing over the Miocene Climate Optimum, *Sci Bull (Beijing)*, 69, 823-832,
425 10.1016/j.scib.2023.12.052, 2024.

426 Lunt, D. J., Valdes, P. J., Haywood, A., and Rutt, I. C.: Closure of the Panama Seaway during the Pliocene:
427 implications for climate and Northern Hemisphere glaciation, *Climate Dynamics*, 30, 1-18, 10.1007/s00382-
428 007-0265-6, 2008.

429 Lunt, D. J., Haywood, A. M., Schmidt, G. A., Salzmann, U., Valdes, P. J., Dowsett, H. J., and Loftson, C. A.: On the
430 causes of mid-Pliocene warmth and polar amplification, *Earth and Planetary Science Letters*, 321-322, 128-
431 138, <https://doi.org/10.1016/j.epsl.2011.12.042>, 2012.

432 Marsicek, J., Shuman, B. N., Bartlein, P. J., Shafer, S. L., and Brewer, S.: Reconciling divergent trends and

433 millennial variations in Holocene temperatures, *Nature*, 554, 92-96, 10.1038/nature25464, 2018.

434 Milanković, M.: Canon of insolation and the ice-age problem Belgrade, 1941, *Kanon der Erdbestrahlung und*
435 *seine Anwendung auf das Eiszeitenproblem*. English, xxiii, 484 p., [English translation by Israel Porgram for
436 Scientific Translation and published by the U.S. Dept. of Commerce and national Science Foundation.],
437 Jerusalem, xxiii, 484 p. pp.1941.

438 Naish, T., Powell, R., Levy, R., Wilson, G., Scherer, R., Talarico, F., Krissek, L., Niessen, F., Pompilio, M., Wilson, T.,
439 Carter, L., DeConto, R., Huybers, P., McKay, R., Pollard, D., Ross, J., Winter, D., Barrett, P., Browne, G., Cody, R.,
440 Cowan, E., Crampton, J., Dunbar, G., Dunbar, N., Florindo, F., Gebhardt, C., Graham, I., Hannah, M., Hansaraj,
441 D., Harwood, D., Helling, D., Henrys, S., Hinnov, L., Kuhn, G., Kyle, P., Laufer, A., Maffioli, P., Mogens, D.,
442 Mandernack, K., McIntosh, W., Millan, C., Morin, R., Ohneiser, C., Paulsen, T., Persico, D., Raine, I., Reed, J.,
443 Riesselman, C., Sagnotti, L., Schmitt, D., Sjunneskog, C., Strong, P., Taviani, M., Vogel, S., Wilch, T., and Williams,
444 T.: Obliquity-paced Pliocene West Antarctic ice sheet oscillations, *Nature*, 458, 322-328, 10.1038/nature07867,
445 2009.

446 Reichgelt, T., Baumgartner, A., Feng, R., and Willard, D. A.: Poleward amplification, seasonal rainfall and forest
447 heterogeneity in the Miocene of the eastern USA, *Global and Planetary Change*, 222,
448 10.1016/j.gloplacha.2023.104073, 2023.

449 Sarr, A.-C., Donnadiou, Y., Bolton, C. T., Ladant, J.-B., Licht, A., Fluteau, F., Laugié, M., Tardif, D., and Dupont-
450 Nivet, G.: Neogene South Asian monsoon rainfall and wind histories diverged due to topographic effects,
451 *Nature Geoscience*, 15, 314-319, 10.1038/s41561-022-00919-0, 2022.

452 Setty, S., Cramwinckel, M. J., van Nes, E. H., van de Leemput, I. A., Dijkstra, H. A., Lourens, L. J., Scheffer, M., and
453 Sluijs, A.: Loss of Earth system resilience during early Eocene transient global warming events, *Science Advances*,
454 9, eade5466, 10.1126/sciadv.ade5466, 2023.

455 Steinthorsdottir, M., Coxall, H. K., de Boer, A. M., Huber, M., Barbolini, N., Bradshaw, C. D., Burls, N. J., Feakins,
456 S. J., Gasson, E., Henderiks, J., Holbourn, A. E., Kiel, S., Kohn, M. J., Knorr, G., Kürschner, W. M., Lear, C. H.,
457 Liebrand, D., Lunt, D. J., Mörs, T., Pearson, P. N., Pound, M. J., Stoll, H., and Strömberg, C. A. E.: The Miocene:
458 The Future of the Past, *Paleoceanography and Paleoclimatology*, 36, 10.1029/2020pa004037, 2021.

459 Tian, J., Yang, M., Lyle, M. W., Wilkens, R., and Shackford, J. K.: Obliquity and long eccentricity pacing of the
460 Middle Miocene climate transition, *Geochemistry, Geophysics, Geosystems*, 14, 1740-1755,
461 10.1002/ggge.20108, 2013.

462 Utescher, T., Ivanov, D., Harzhauser, M., Bozukov, V., Ashraf, A. R., Rolf, C., Urbat, M., and Mosbrugger, V.: Cyclic
463 climate and vegetation change in the late Miocene of Western Bulgaria, *Palaeogeography, Palaeoclimatology,*
464 *Palaeoecology*, 272, 99-114, 10.1016/j.palaeo.2008.11.014, 2009.

465 van Peer, T. E., Liebrand, D., Taylor, V. E., Brzelinski, S., Wolf, I., Bornemann, A., Friedrich, O., Bohaty, S. M., Xuan,
466 C., Lippert, P. C., and Wilson, P. A.: Eccentricity pacing and rapid termination of the early Antarctic ice ages, *Nat*
467 *Commun*, 15, 10600, 10.1038/s41467-024-54186-1, 2024.

468 Wang, Y., Yu, Z., Lin, P., Liu, H., Jin, J., Li, L., Tang, Y., Dong, L., Chen, K., Li, Y., Yang, Q., Ding, M., Meng, Y., Zhao,
469 B., Wei, J., Ma, J., and Sun, Z.: FGOALS-g3 Model Datasets for CMIP6 Flux-Anomaly-Forced Model
470 Intercomparison Project, *Advances in Atmospheric Sciences*, 37, 1093-1101, 10.1007/s00376-020-2045-8,
471 2020.

472 Wei, J., Liu, H., Zhao, Y., Lin, P., Yu, Z., Li, L., Xie, J., and Duan, A.: Simulation of the climate and ocean circulations
473 in the Middle Miocene Climate Optimum by a coupled model FGOALS-g3, *Palaeogeography, Palaeoclimatology,*
474 *Palaeoecology*, 617, 10.1016/j.palaeo.2023.111509, 2023.

475 Westerhold, T., Marwan, N., Drury, A. J., Liebrand, D., Agnini, C., Anagnostou, E., Barnet, J. S. K., Bohaty, S. M.,
476 De Vleeschouwer, D., Florindo, F., Frederichs, T., Hodell, D. A., Holbourn, A. E., Kroon, D., Lauretano, V., Littler,
477 K., Lourens, L. J., Lyle, M., Pälike, H., Röhl, U., Tian, J., Wilkens, R. H., Wilson, P. A., and Zachos, J. C.: An
478 astronomically dated record of Earth's climate and its predictability over the last 66 million years, 369, 1383-
479 1387, doi:10.1126/science.aba6853, 2020.

480 Yin, Q., and Berger, A.: Individual contribution of insolation and CO₂ to the interglacial climates of the past
481 800,000 years, *Climate Dynamics*, 38, 709-724, 10.1007/s00382-011-1013-5, 2012.
482 Yin, Q.: Insolation-induced mid-Brunhes transition in Southern Ocean ventilation and deep-ocean
483 temperature, *Nature*, 494, 222-225, 10.1038/nature11790, 2013.
484 Zhang, Y. (2025, June 12). *Miocene_orb*. <https://doi.org/10.17605/OSF.IO/ZRC48>
485 Zhang, Z., Ramstein, G., Schuster, M., Li, C., Contoux, C., and Yan, Q.: Aridification of the Sahara desert caused
486 by Tethys Sea shrinkage during the Late Miocene, *Nature*, 513, 401-404, 10.1038/nature13705, 2014.
487 Zheng, W., Yu, Y., Luan, Y., Zhao, S., He, B., Dong, L., Song, M., Lin, P., and Liu, H.: CAS-FGOALS Datasets for
488 the Two Interglacial Epochs of the Holocene and the Last Interglacial in PMIP4, *Advances in Atmospheric*
489 *Sciences*, 37, 1034-1044, 10.1007/s00376-020-9290-8, 2020.

490